INFRARED DARK CLOUDS IN THE SMALL MAGELLANIC CLOUD?

MIN-YOUNG LEE[1], SNEŽANA STANIMIROVIĆ[1], JÜRGEN OTT[2], JACCO TH. VAN LOON[3], ALBERTO D. BOLATTO[4], PAUL A. JONES[5,6], MARIA R. CUNNINGHAM[5], KATHRYN E. DEVINE[1], AND JOANA M. OLIVEIRA[3]

[1] Department of Astronomy, University of Wisconsin-Madison, 475 North Charter Street, Madison, WI 53706, USA; lee@astro.wisc.edu, sstanimi@astro.wisc.edu, devine@astro.wisc.edu
[2] National Radio Astronomy Observatory, 520 Edgemont Road, Charlotteville, VA 22903, USA; jott@nrao.edu
[3] Astrophysics Group, Lennard Jones Laboratories, Keele University, Staffordshire, ST5 5BG, UK; jacco@astro.keele.ac.uk, joana@astro.keele.ac.uk
[4] Department of Astronomy and Laboratory for Millimeter-wave Astronomy, University of Maryland, College Park, MD 20742, USA; bolatto@astro.umd.edu
[5] School of Physics, University of New South Wales, Sydney, UNSW 2052, Australia; pjones@phys.unsw.edu.au, maria.cunningham@unsw.edu.au
[6] Departamento de Astronomia, Universidad de Chile, Casilla 36-D, Santiago, Chile

ABSTRACT

We have applied the unsharp-masking technique to the 24 μm image of the Small Magellanic Cloud (SMC), obtained with the *Spitzer Space Telescope*, to search for high-extinction regions. This technique has been used to locate very dense and cold interstellar clouds in the Galaxy, particularly infrared dark clouds (IRDCs). Fifty-five candidate regions of high extinction, namely, high-contrast regions (HCRs), have been identified from the generated decremental contrast image of the SMC. Most HCRs are located in the southern bar region and mainly distributed in the outskirts of CO clouds, but most likely contain a significant amount of H_2. HCRs have a peak contrast at 24 μm of 2%–2.5% and a size of 8–14 pc. This corresponds to the size of typical and large Galactic IRDCs, but Galactic IRDCs are 2–3 times darker at 24 μm than our HCRs. To constrain the physical properties of the HCRs, we have performed NH_3, N_2H^+, HNC, HCO^+, and HCN observations toward one of the HCRs, HCR LIRS36–east, using the Australia Telescope Compact Array and the Mopra single-dish radio telescope. We did not detect any molecular line emission, however, our upper limits to the column densities of molecular species suggest that HCRs are most likely moderately dense with $n \sim 10^3$ cm^{-3}. This volume density is in agreement with predictions for the cool atomic phase in low-metallicity environments. We suggest that HCRs may be tracing clouds at the transition from atomic to molecule-dominated medium, and could be a powerful way to study early stages of gas condensation in low-metallicity galaxies. Alternatively, if made up of dense molecular clumps < 0.5 pc in size, HCRs could be counterparts of Galactic IRDCs, and/or regions with highly unusual abundance of very small dust grains.

Key words: galaxies: ISM – infrared: galaxies – ISM: clouds – ISM: molecules – Magellanic Clouds – radio lines: ISM

Online-only material: color figure

1. INTRODUCTION

The discovery of infrared dark clouds (IRDCs) through the *Infrared Space Observatory* (*ISO*) and the *Midcourse Space Experiment* (*MSX*) surveys of the Galactic plane (Pérault et al. 1996; Carey et al. 1998; Egan et al. 1998) opened a new window for studies of the dense and cold interstellar medium (ISM). IRDCs, a new class of interstellar clouds, are seen as dark extinction features against the bright Galactic background at mid-infrared (mid-IR) wavelengths. In-depth studies with images obtained by the *Infrared Astronomical Satellite* (*IRAS*) and the *MSX* showed that IRDCs are opaque at wavelengths from 7 to 100 μm (Egan et al. 1998). Millimeter and submillimeter observations confirmed that IRDCs are dense ($n > 10^5$ cm^{-3}) and cold ($T_{gas} < 20$ K), and have high H_2 column densities (10^{23-25} cm^{-2}; Carey et al. 1998, 2000; Rathborne et al. 2005).

A new approach for studying the dense and cold ISM, based on the unsharp-masking technique, may be particularly useful for low-metallicity environments where, due to a low shielding ability, molecules can survive only in dense cores (Elmegreen 1989) and thus it is extremely difficult to find them with blind searches. High-sensitivity and high-resolution IR images, obtained with the *Spitzer Space Telescope* (*Spitzer* throughout this paper; Werner et al. 2004), are suitable for searching for dark clouds at mid-IR wavelengths to locate potential dense molecular clouds. Motivated by the recent *Spitzer* observations of the Small Magellanic Cloud (SMC; Bolatto et al. 2007), we undertook the first search for IR dark clouds in the SMC.

One of the closest neighbors of the Galaxy, the SMC is a low-mass ($M_{dyn} \sim 2.4 \times 10^9$ $M_\odot$; Stanimirović et al. 2004), gas-rich (Staveley-Smith et al. 1998), dwarf irregular galaxy at a distance of approximately 60 kpc[7] from Earth (Westerlund 1991). Like its companion galaxy, the Large Magellanic Cloud (LMC), the SMC has a number of active star-forming regions. Most of the star formation activity in the SMC is concentrated in the feature known as the bar. The SMC bar contains most of the dense gas as well. Rubio et al. (1991) pointed out the difference in the star formation activity along the bar, with the southwest (SW) region being more active and containing a large number of young objects which correlate well with CO clouds, while the northeast (NE) region containing only smaller CO clouds with almost no association with young stellar objects. The second prominent large-scale feature in the SMC, the wing, is located to the southeast (SE) of the SMC and contains young stellar components (e.g., N83/N84 region) which imply recent star formation (Westerlund & Glaspey 1971; Kunkel 1980).

The interstellar environment in the SMC is very different from that in the Galaxy. The SMC has a much lower heavy element abundance ($Z \sim 0.2 Z_\odot$; Dufour 1975) and an interstellar

---

[7] Throughout this paper, we assume a distance to the SMC of 60 kpc.

UV radiation field (ISRF) 4–10 times higher than that in the solar neighborhood (Lequeux 1979; Vangioni-Flam et al. 1980; Azzopardi et al. 1988). Hence, the SMC provides a unique laboratory to study how different galactic interstellar environments affect properties and evolution of the ISM. In addition, the SMC is the closest local example of a relatively primitive ISM and provides a stepping stone in our understanding of the ISM in high-redshift galaxies.

While many authors have investigated properties of molecular gas in the SMC based on CO observations, only a few measurements of molecular species other than CO exist (Chin et al. 1998; Heikkilä et al. 1999). Rubio et al. (1993) and Lequeux et al. (1994) analyzed CO data obtained by the Swedish-ESO Submillimeter Telescope (SEST) and found that CO(1–0) emission is deficient in the SMC by a factor of 10–20 relative to the Galaxy. Their results also showed that CO clouds in the SMC are clumpy with a surface filling factor lower than for Galactic clouds. In addition, several studies suggested that the CO emission is found only in dense cores, and that molecular hydrogen (H_2) may have a more extended distribution. Mizuno et al. (2001) compared CO luminosities for clouds observed by both NANTEN (angular resolution $\sim 2'.6$) and SEST (angular resolution $\sim 45''$) and concluded that the CO emission is highly clumped, with no diffuse CO emission in the intercloud medium. Rubio et al. (2000) performed observations of the $v = (1-0)S(1)$ line of H_2 toward N66 and found that CO molecules only exist in regions with A_V larger than 1 mag, compared to 0.1 mag or less for the $v = (1-0)S(1)$ line of H_2. Using the *Spitzer* 24, 70, and 160 μm images, Leroy et al. (2007) constructed the H_2 surface density map under the assumption that all excess of far-IR emission, relative to the observed H I emission (corrected for self-absorption), comes from the H_2 component. They estimated $M_{H_2} = 3.2 \times 10^7 \ M_\odot$ and suggested that H_2 is on average 1–3 times more extended than CO.[8]

Several studies have used IR emission to explore properties of dust in the SMC. Sauvage et al. (1990) studied the effects of stellar age and metallicity on the IR emission in the Magellanic Clouds and found that there is a decrease of the 12 μm flux as a function of metallicity, which indicates a relative underabundance of the polycyclic aromatic hydrocarbons (PAHs) compared to the large grain population. Similarly, Stanimirović et al. (2000) suggested that PAH molecules and very small grains (VSGs) contribute little to the dust emission at wavelengths longer than 45 μm, based on *IRAS* images of the SMC. On the other hand, the recent LMC study with the Surveying the Agents of a Galaxy's Evolution (SAGE) data suggested that the 70 μm excess observed in the spectral energy distributions (SEDs) of both the LMC and SMC could be due to the abundant large VSGs produced through erosion of larger grains in the diffuse medium (Bernard et al. 2008).

The main goal of this study is to search for high-extinction regions at mid-IR wavelengths in the SMC by applying the unsharp-masking technique. By obtaining further molecular line observations, we aim at constraining physical properties of these regions. The *Spitzer* 24 μm image used for this study was obtained as part of the S^{3}MC survey (Bolatto et al. 2007) and has an excellent spatial resolution (1.7 pc) high enough to disentangle individual molecular clouds.

This paper is organized as follows. In Section 2, we use the *Spitzer* 24 μm image of the SMC to generate the decre-

mental contrast image and search for high-extinction regions (high-contrast regions; HCRs throughout this paper). In Section 3, overall properties of identified HCRs are investigated. In Section 4, we examine characteristics of several selected HCRs using the available multi-wavelength data. In Section 5, we present our observations of NH$_3$, N$_2$H$^+$, HNC, HCO$^+$, and HCN toward one HCR (named as HCR LIRS36–east) and derive upper limits to the column densities of observed molecular species. Constraints on the physical properties and potential origins of HCRs are discussed in Section 6. We summarize our main findings in Section 7.

2. SEARCH FOR HIGH-EXTINCTION REGIONS IN THE SMC: THE 24 μm CONTRAST IMAGE

In the Galaxy, high-extinction regions (like IRDCs) are identified as silhouettes against the diffuse Galactic background at mid-IR wavelengths that easily stand out when an unsharp-masking technique is applied (e.g., Simon et al. 2006a). Assuming that similar reasoning will apply in the SMC, we have searched for fractional decrements in the *Spitzer* 24 μm image. We followed the method of Simon et al. (2006a) who identified and cataloged 10,931 Galactic IRDC candidates by searching for contiguous regions of high contrast with respect to the background of the *MSX* 8.3 μm image. Since the small dust grains, especially PAHs are less abundant in the SMC than in the Galaxy (Sauvage et al. 1990; Stanimirović et al. 2000), the 8 μm image of the SMC obtained with the *Spitzer* (Bolatto et al. 2007) does not show significant diffuse emission. In addition, the diffuse 8 μm emission is mainly concentrated around H II regions, providing very little diffuse IR background for unsharp masking. The diffuse IR emission at 24 μm is more pronounced, providing the opportunity to look for local spatial variations. In addition, at least one sharp silhouette is noticeable by eye in the southern bar region, giving us confidence that this method may reveal some interesting structures.

The *Spitzer* 24 μm image has an angular resolution of $6''$ and this corresponds to a linear size of 1.7 pc at a distance of 60 kpc. The 24 μm wave band is sensitive to continuum emission from PAHs and VSGs ($a \lesssim 0.005 \ \mu$m) but much of the 24 μm emission in the SMC is expected to come from stochastically heated ($\sim$150 K) VSGs. For example, Madden et al. (2006) showed that the mid-IR emission from N66 is dominated by VSGs. These authors used one of ISOCAM bands, covering the wavelength range from 12 to 18 μm, and estimated that 85%–95% of the IR flux comes from VSGs. To search for high-extinction regions, we first determined the diffuse IR background at 24 μm and then derived the decremental contrasts against this background.

2.1. Determining the Diffuse 24 μm Background

We assumed that the *Spitzer* 24 μm image, apart from bright emission from star-forming regions and point sources, consists of the diffuse IR background against which high-extinction clouds are superposed. To determine the background, we smoothed the *Spitzer* 24 μm image using the technique of spatial median filtering. The median filtering size must be larger than the typical size of high-extinction regions, but small enough to follow the spatial distribution of the background. Typical IRDCs in the Galaxy are smaller than 10 pc (or $0'.6$, which is $\sim$10 pixels in the 24 μm image; one pixel corresponds to 1×10^{-3} deg), and we used this as the absolute minimal size for our smoothing kernel. On the other hand, as the spatial variation

---

[8] It is important to point out that the excess far-IR emission could result from an increased far-IR emissivity, possibly due to growth of icy mantles on the surface of dust grains, and/or spatial variations of the dust-to-gas ratio.
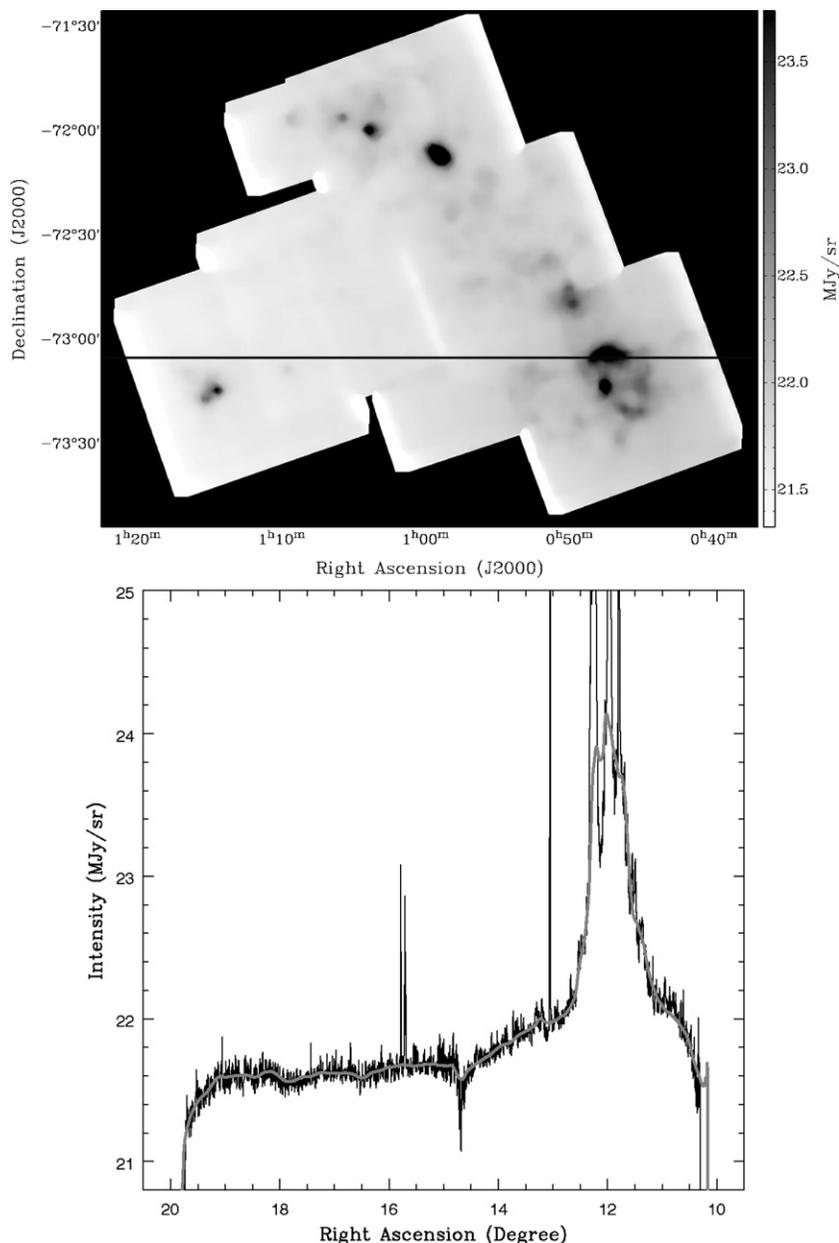
Figure 1. Top: the IR background obtained using the median filtering with 63 pixels. The horizontal line shows the location of the profile shown in the bottom panel. Bottom: the profile of the IR background (gray) superposed on the original *Spitzer* image data (black). Foreground emission (a sum of zodiacal light, Galactic dust emission, and small cosmic IR background, ∼21.6 MJy sr^{-1}) is not subtracted. The gap at R.A. = 15° is due to a small gap between different mosaic pieces of the *Spitzer* 24 μm image.

of the background at 24 μm is typically larger than 100 pc (or 6′, which is ∼95 pixels in the 24 μm image), the median filtering size must be smaller than 95 pixels. We examined the spatial variation of the background at 24 μm by obtaining profiles across the *Spitzer* image at various positions. We varied the median filtering size from about 33–95 pixels and selected the kernel with 63 pixels (or 66 pc) as providing the best estimate of the IR background.

Figure 1 shows the estimated 24 μm background image (top) and a profile along the *x*-axis of the background image superposed on the original 24 μm data (bottom). For the median kernel with 63 pixels, the diffuse background emission contributes only 27% of the total 24 μm emission. Most of the 24 μm emission comes from H II regions, in particular, those in the southern bar region. The ratio of diffuse to total 24 μm

emission varies from 23% in the NE portion of the bar, to 31% in the SW portion of the bar.

2.2. The Contrast Image

After determining the background, we generated the contrast image by subtracting the *Spitzer* 24 μm image from the estimated background and then dividing the residual image by the background image, contrast = (background − original image)/background. By this definition, regions having lower surface brightness against the background will have positive contrasts. The H II regions have negative contrasts as their IR emission is higher than the IR background and we exclude them from further analysis. Our detection method is therefore limited to positive contrasts and we are essentially blind to
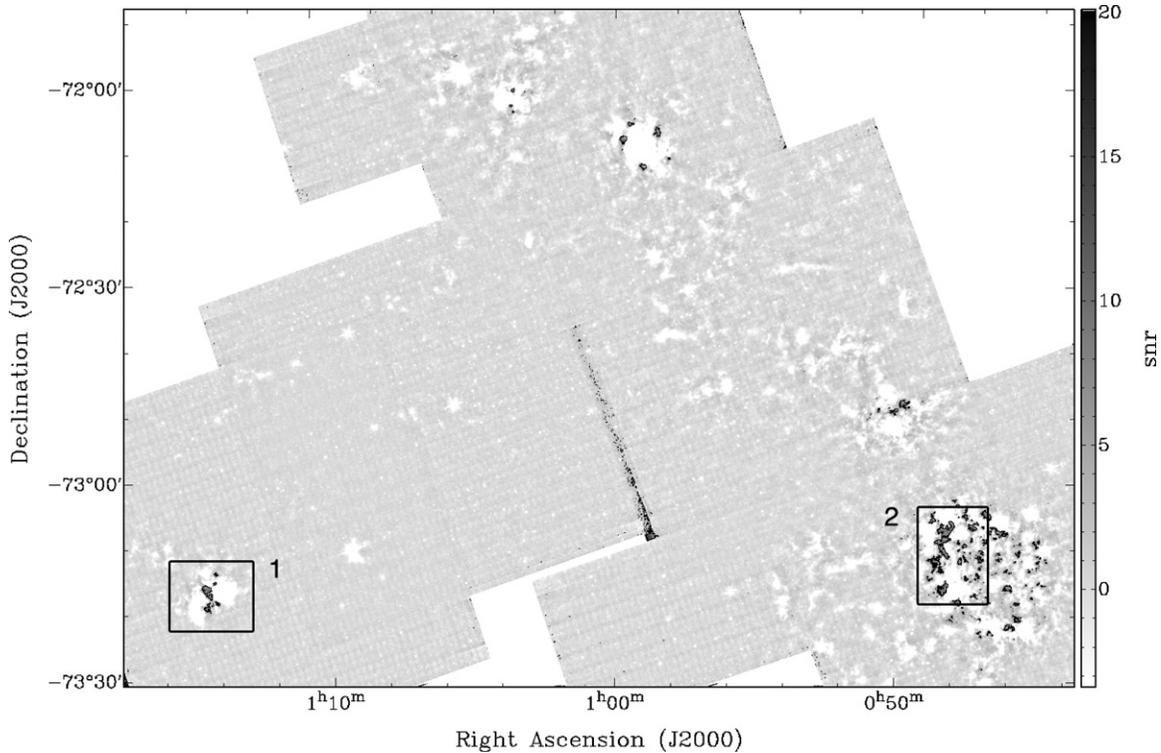
Figure 2. Signal-to-noise ratio image derived from the *Spitzer* 24 μm image. The black contours are at 5σ level. H II regions and stars have values higher than the IR background and appear as negative (white) pixels in this image. Regions with intensity lower than the IR background (HCRs) appear as positive (dark) features in this image. Boxes 1 and 2 show selected subregions for Figures 5 and 6 (box 1: Figure 5; box 2: Figure 6).

high-extinction regions that may be present within the boundaries of H II regions.

The (positive) contrasts are typically very small and range from 0% to 4%. To estimate the significance of contrasts, we derived the signal-to-noise ratio image. The signal-to-noise ratio here is defined by the ratio of the contrast to its error ($c/\Delta c$). The contrast error (Δc) for a particular pixel was calculated by dividing the average 1σ noise level in the 24 μm image by the pixel value in the background image. We have assumed a constant value for the 1σ noise level of 0.06 MJy sr^{-1} by considering several emission-free regions in the image. The derived signal-to-noise ratio image is shown in Figure 2.

Figure 3 shows a histogram of pixel values from the signal-to-noise ratio image for the SMC SW bar. For small values ($< 3\sigma$), this distribution can be well fitted with a Gaussian function, suggesting that a majority of pixels have low significance and are purely due to Gaussian noise. However, the distribution has a significant tail, peaking around 4σ, and suggesting that a certain fraction of pixels with high-significance deviate from the Gaussian statistics and could represent real features.

### 2.3. Selection of High-contrast Regions (HCRs)

Figure 2 shows many small and large features with significant fractional decrements of the 24 μm intensity relative to the IR background. Figure 3 shows a significant fraction of pixels with $c > 3\sigma$. To select reliable HCRs, we take a conservative approach and search for contiguous regions with contrasts higher than 5σ. This is mainly motivated by a high likelihood of spurious detections at low contrasts (discussed below). In addition, we require HCRs to be extended and contain at least 9–10 pixels. This corresponds to twice the full width at half-maximum (FWHM) beam solid angle of the *Spitzer* at 24 μm

($2\Omega = 2.26 \times (6'')^2 = 81$ arcsec$^2 \sim 3 \times 3$ pixels). Therefore, the smallest clouds we are sensitive to have a size of $\sim$3 pc. This is similar to the typical size of Galactic IRDCs, $\sim$4 pc (Simon et al. 2006b), although Galactic IRDCs can range in size from 0.4 to 10 pc (Pillai et al. 2006; Frieswijk et al. 2007). We are therefore sensitive to the counterparts of typical and large Galactic IRDCs. By these criteria, 55 candidate HCRs (39 from the southern bar, 6 from the eastern wing, and 10 from the northern bar) were identified.

However, it is possible that some HCRs are spurious and do not trace regions of high extinction due to the following limitations of our method.

(1) The HCRs have peak contrasts up to 4%, which is lower than what is found for Galactic IR images (see Section 3 for details). For the Galactic HCRs, Simon et al. (2006a) and Jackson et al. (2008) showed that higher contrast candidates have high CS(2–1) line ($n_{\rm crit} = 7 \times 10^5$ cm^{-3}) detection rates and are therefore prime regions for being real IRDCs. For contrasts of $c_8 = 20\%$–40% at 8 μm, which corresponds to $c_{24} = 4\%$–10% at 24 μm (assuming the relation $A_\lambda \propto \lambda^{-1.7}$ in the near-IR regime; Mathis 1990), their detection rate of CS(2–1) emission was 50%, while for $c_8 > 60\%$, which corresponds to $c_{24} > 20\%$, the detection rate increased to nearly 100%. Based on these studies, HCRs with $c_{24} < 4\%$ are expected to have high likelihood of being spurious detections in terms of being tracers of regions with the highest extinction.

(2) To be detected, HCRs need to lie in front of the bulk of diffuse IR emission. The SMC has been postulated to have a significant line-of-sight depth (e.g., Mathewson et al. 1986; Welch et al. 1987), which complicates the detection of HCRs. HCRs in the parts of the SMC with lower line-of-sight depth (NW) and at a near distance will be easier to find, while HCRs in regions with a larger depth (SW) will tend to be filled by
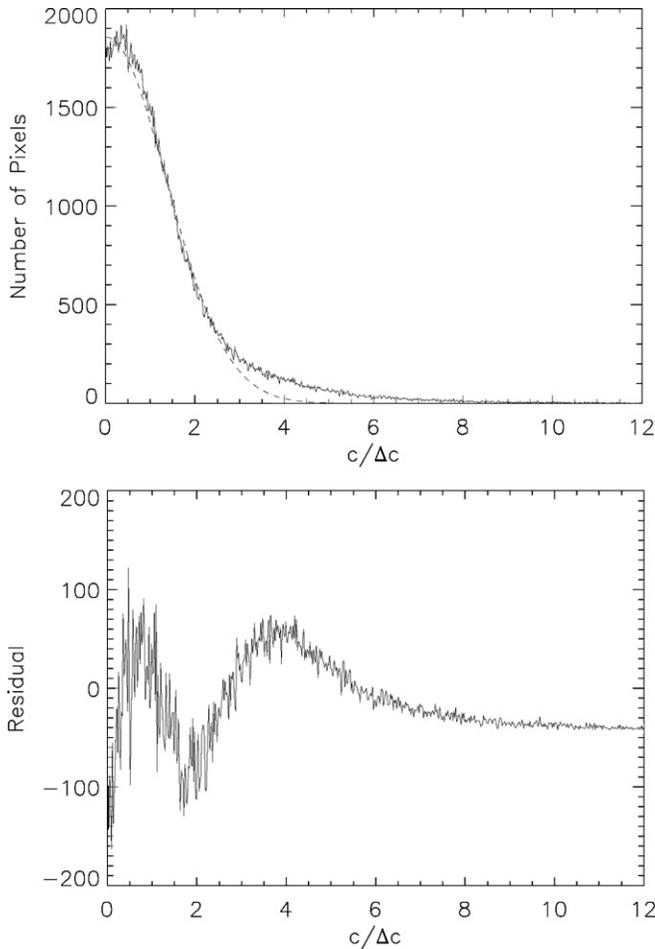
Figure 3. Top: the histogram of the signal-to-noise ratio image for the SMC SW bar region. The fitted Gaussian function is shown with the dashed line. Bottom: the residuals after removing the Gaussian fit. From about 3σ, there is a certain fraction of pixels with significant deviation from the Gaussian statistics.

the foreground emission and hard to detect (see Section 3 for details).

(3) The uncertainty and fluctuations in the IR background, especially close to complex H II regions, affect the reliability of HCRs. It has been pointed out by several studies that the unsharp-masking technique cannot distinguish voids in regions of complex emission from actual extinction features. This results in false detections and the exact reliability of the method is best constrained through observations of molecular lines (Jackson et al. 2008).

After taking into consideration all selection effects, we stress that our detection method is blind to high-extinction regions within the boundaries of H II regions and is biased toward the outskirts of H II regions where the diffuse IR emission is stronger than in outer parts of the SMC. Considering that HCRs with very high contrasts in the Galaxy show a high detection rate in molecular line observations, we focus in this paper primarily on several selected regions with the highest contrasts, and therefore the highest likelihood of being real. The best approach for checking the reliability of HCRs is through a detection and morphological matching of molecular line emission/continuum data which we attempt in Sections 4 and 5.

3. OVERALL PROPERTIES OF HCRs

Figure 2 shows the spatial distribution of HCRs, with most of them (39 out of 55) being in the SW portion of the SMC

bar. Other SMC regions contain only a few HCRs. While the exact line-of-sight depth of the SMC is uncertain, most studies agree that the depth is higher in the SW portion of the bar than in the NE region (Mathewson et al. 1986; Groenewegen 2000; Subramanian & Subramaniam 2009). Based on our selection bias discussed in Section 2.3, this effect would result in a smaller number of HCRs in the SW region, yet we see an opposite trend. The distribution of H II regions seen in Figure 2 (as negative, white pixels) is relatively uniform along the bar; no strong north–south asymmetry is observed. In addition, the fraction of IR background emission relative to the total emission is not very different between the NE and the SW, 23% versus 31%, respectively. This all suggests that the highly inhomogeneous spatial distribution of HCRs, with a large abundance of HCRs in the SW, is not a selection bias but is an intrinsic property.

It is interesting to note that the large disproportion in the spatial distribution of HCRs is qualitatively similar to the spatial distribution of CO clouds by Mizuno et al. (2001). Most of the CO clouds (ranging in size from 50 to 160 pc) are located in the SW bar, with only a few sporadic clouds being found elsewhere. The total area of CO clouds corresponds to ~5% for the NE and ~11% for the SW (Mizuno et al. 2001). Young emission objects (e.g., H II regions with embedded OB associations and star clusters) tracing star formation in the range < 5–6 Myr were found to be well correlated with CO clouds, while emissionless objects (e.g., emissionless OB associations and star clusters of ages ~6–100 Myr) do not show any particular association with CO clouds. This suggests that HCRs are intimately connected with CO clouds and active (more recent) sites of star formation.
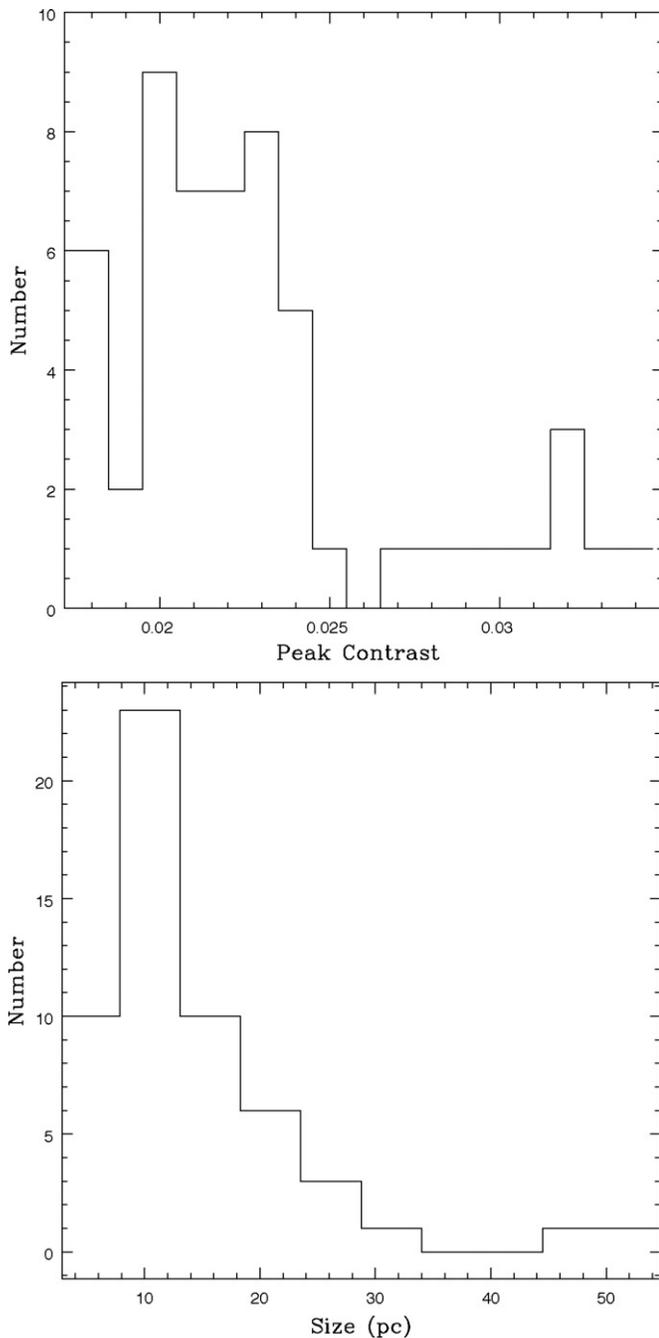
In Figure 4, we present two histograms showing the peak contrast and size distribution of selected 55 HCRs. The peak contrast of HCRs ranges from 1.7% to 3.5% and peaks at 2%–2.5%. The distribution of peak contrasts of Galactic IRDCs at 8 μm is approximately a power aw, with a peak around 15%–20% (full range 10%–60%; Simon et al. 2006a). After converting this to the expected extinction at 24 μm (using the relation $A_\lambda \propto \lambda^{-1.7}$ in the near-IR regime; Mathis 1990), HCRs in the SMC have a peak contrast a factor of 2–3 lower than Galactic IRDCs.

The size distribution in Figure 4 (bottom) shows that 80% of the selected HCRs have a size in the range from 3 to 18 pc (to estimate cloud size we counted the number of pixels within the HCRs and then assumed simply spherically symmetric clouds). The lower limit of this size distribution is set by our selection criteria and resolution. There is a strong peak at 8–14 pc and a tail going all the way to ~50 pc. Galactic IRDCs have diameters of 0.4–10 pc (Pillai et al. 2006; Frieswijk et al. 2007), with a typical size of ~4 pc (Simon et al. 2006b). This is much smaller than the average diameter of giant molecular clouds (GMCs) in the Galaxy, which is about 50 pc. HCRs in the SMC therefore, sizewise, are significantly smaller than the GMCs in either the Galaxy or the SMC and similar to counterparts of typical and large Galactic IRDCs.

Under the assumption that HCRs are entirely due to the extinction of IR background emission at 24 μm, we can use the following simple radiative transfer equation to estimate their optical depth:

$$c = \beta(1 - e^{-\tau}), \qquad (1)$$

where c is the peak contrast, $\beta = I_{\rm bh}/I_{\rm bg}$ is the fraction of IR emission behind the HCR relative to the total IR background emission along the line of sight, and τ is the optical depth at 24 μm. By definition $\beta \leqslant 1$, $\beta = 1$ if HCRs are at the front of the SMC and $\beta = 0.5$ if HCRs are in the middle

Figure 4. Top: the histogram of peak contrasts of selected 55 HCRs. Signal-to-noise ratio > 5 was used for the selection. Bottom: the histogram of sizes of selected 55 HCRs. Regions larger than 3 pc were identified as HCRs.

highly unlikely to observe HCRs with such low β values. On the other hand, if HCRs are at the front of the SMC with $\beta = 1$, the estimated A_V would be slightly lower, 0.5–0.6 mag. However, using the H I surface density map (Stanimirović et al. 1999), which has a linear resolution of 30 pc, and applying the relation $N(\text{H I})/A_V = (13.18 \pm 1.02) \times 10^{21}$ established for the SMC bar region (Gordon et al. 2003), we estimate the expected extinction of $A_V = 0.8$–1 mag in the direction of HCRs. This is a lower limit as denser regions are most likely smaller than 30 pc. This suggests that $\beta = 1$ assumption most likely underestimates the amount of extinction, and therefore we assume $\beta = 0.5$ and $A_V \sim 1$ mag throughout the paper.

Using the H_2 surface density map of Leroy et al. (2007), we estimated H_2 surface densities of the HCRs, $\Sigma_{H_2} = 60$–$180\,M_\odot$ pc^{-2}. Molecular peaks in the SMC are typically found to have only slightly higher surface densities, $\Sigma_{H_2} = 100$–$200\,M_\odot$ pc^{-2} (Leroy et al. 2007), suggesting that HCRs contain a significant amount of H_2. Interestingly, contributions from H I and H_2 to the total hydrogen column density are roughly similar, which was also noted for the SMC as a whole by Oliveira (2009).

We conclude that the global properties of the HCRs suggest they are related to recent sites of star formation, and have sizes similar or larger than those of Galactic IRDCs. The peak contrasts of HCRs, $A_V \sim 1$ mag, and the estimated H_2 surface density suggest regions of moderately high density.
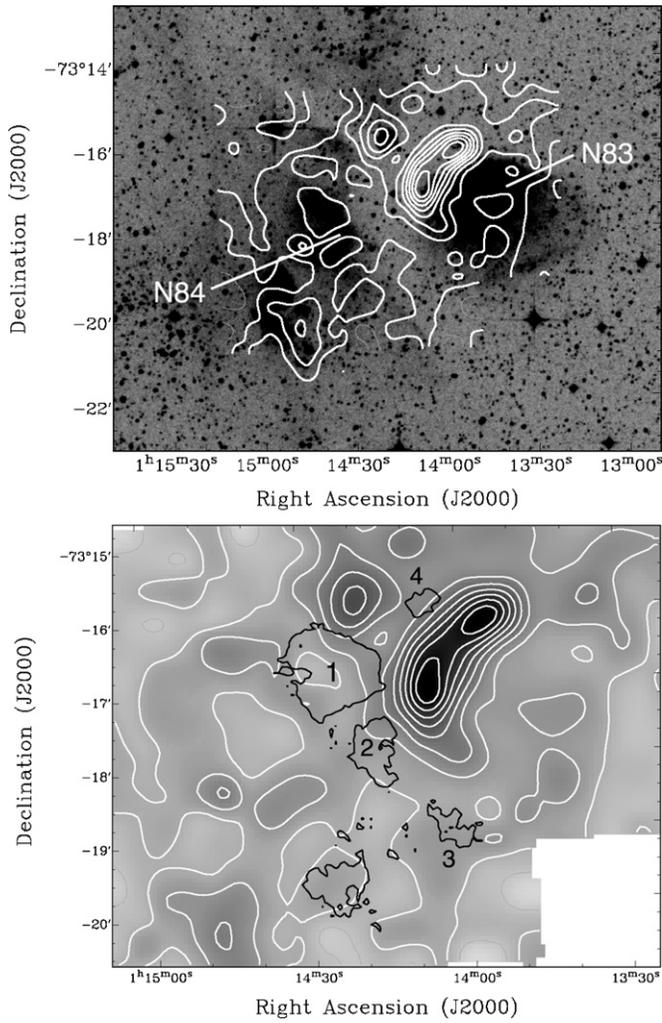
4. SELECTED HCRs

In this section, we focus on several of the most prominent HCRs and examine their properties based on the available multi-wavelength observations.

4.1. HCRs in the N83/N84 Region

N83 and N84 are isolated, relatively active star-forming regions in the SMC wing. The top panel of Figure 5 shows the CO(2–1) integrated intensity map from Bolatto et al. (2003) overlaid on the Digitized Sky Survey (DSS) R-band image of the N83/N84 region. In the bottom panel of Figure 5, selected HCRs are shown as black contours on the background of CO(2–1) intensity map. Four large features with the highest contrasts are labeled. The low abundance of stars between N83 and N84 is clearly seen in the DSS R-band image, which suggests the existence of high-extinction gas. Interestingly, 4 HCRs (size range 6–21 pc), weakly traced by CO(2–1) emission, are identified exactly in this region.

Bolatto et al. (2003) found two distinct regions with anomalously high ratios of CO(2–1)/CO(1–0) (N83 and N84D in Figure 1 of Bolatto et al. 2003). They suggested that this CO emission arises from an ensemble of small ($R \sim 0.1$ pc), moderately dense ($n \sim 10^4$ cm^{-3}), and fairly warm ($T \sim 40$ K) clumps. The 4 HCRs are located between the two regions with high ratios of CO(2–1)/(1–0). This suggests that HCRs may trace gas compressed between N83 and N84. As N83 is an expanding molecular shell, this would give a mechanism for warm CO gas to be swept up and compressed.

Leroy et al. (2009) investigates the relationship between the integrated CO(1–0) and CO(2–1) emission (I_{CO}) and Σ_{H_2} in the N83/N84 region at 10 pc resolution. They find that $I_{\text{CO}(1-0)} = 0$ K km s^{-1} corresponds to roughly $\Sigma_{H_2} = 50$–$150\,M_\odot$ pc^{-2} and interpret this as the presence of an envelope of H_2 with little or no associated CO. Regions with enough high dust shielding ($A_V > 2$ mag; A_V is estimated from the *Spitzer* 160 μm

of the SMC. By assuming $\beta = 0.5$ and using the relation $A_V = A_{24}/0.045$ (based on Figures 1 and 4 of Draine 2003), we obtained $A_V = 1$–1.2 mag for HCRs with $c_{24} = 0.02$–0.025. This is moderately high for the SMC, considering that molecular peaks in the SMC have $A_V = 1$–2 mag (Leroy et al. 2007).

We have considered possible variations in A_V when β varies from 0.1 to 1. For $\beta = 0.1$, the estimated A_V is significantly higher, 5–7 mag. However, it would be very hard to detect HCRs from the far side of the SMC as they would not have much IR background emission to absorb. In addition, even if a HCR at a far distance has a suitable IR background against which to absorb, the dark extinction feature will tend to be filled by the foreground IR emission along the line of sight. It is therefore
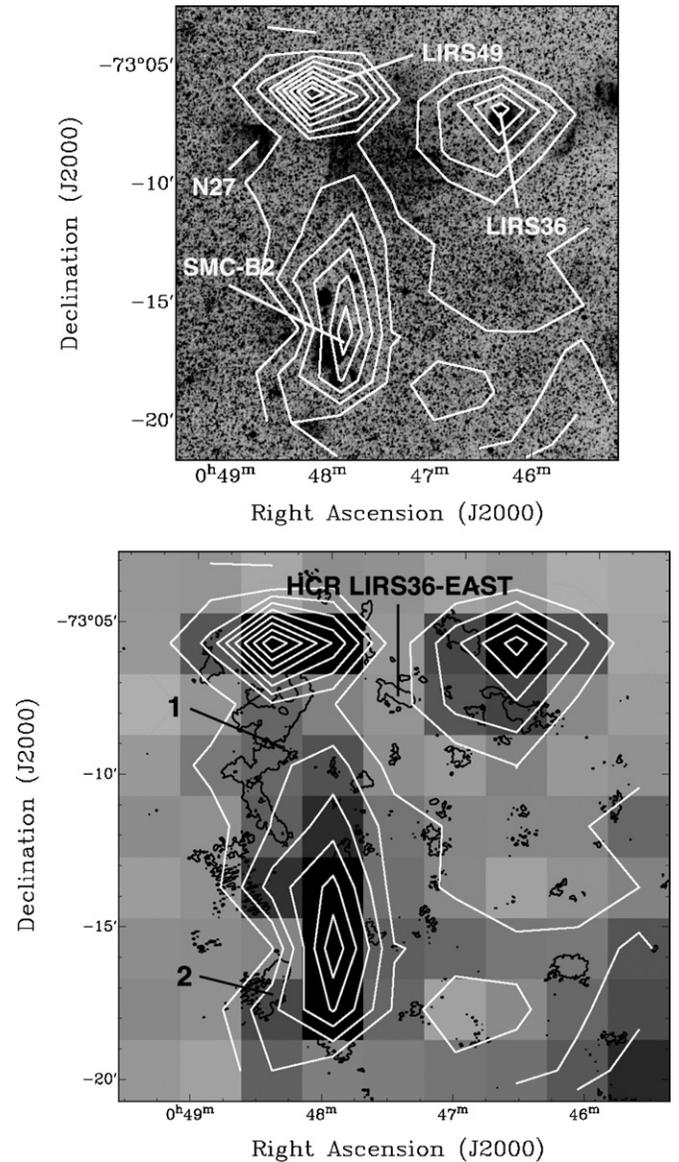
Figure 5. Top: the CO(2–1) integrated intensity map (Bolatto et al. 2003) overlaid on the DSS *R*-band image of the N83/N84 region. The CO contour levels are from 10% to 90% of the peak (0.0045 K km s^{-1}), with a 10% step. Bottom: the four highest contrast features (from 1 to 4 in order of size) are overlaid in black contours on the CO(2–1) integrated intensity map.

image assuming optically thin dust grains) are found to have $I_{CO(1-0)} > 0$ K km s^{-1}. The threshold of $A_V > 2$ mag required for CO survival in the presence of an intense radiation field is in agreement with Lequeux et al.'s (1994) modeling. The 4 HCRs in this region have $\Sigma_{H_2} = 100$–$150\,M_\odot$ pc^{-2}, very little CO, and $A_V = 0.6$–1.5 mag. This is in agreement with properties of CO-weak, H$_2$-dominated envelopes.

In summary, from the studies of Bolatto et al. (2003) and Leroy et al. (2009), we suggest that HCRs in the N83/N84 region most likely trace moderately dense gas ($n \sim 10^4$ cm^{-3} as the critical density for CO(2–1) is $\sim 10^4$ cm^{-3}) in the extended H$_2$-dominated molecular cloud envelope, on spatial scales of 6–20 pc.

4.2. HCRs in the SMC–B2 Region

The SMC–B2 region is located in the southern bar at (α, δ)$_{J2000}$ = (00^h:48^m:01^{s}96, $-73°$:15':38"5). This region contains many HCRs, whose sizes range from 4 to 48 pc. The top panel of Figure 6 shows the CO(1–0) integrated intensity map overlaid on the DSS *R*-band image. In the bottom panel of Figure 6, selected HCRs are shown in black contours with the background of CO(1–0) intensity map. Two large features with


Figure 6. Top: the CO(1–0) integrated intensity map (Mizuno et al. 2001) overlaid on the DSS *R*-band image of the SMC–B2 region. The CO contour levels are from 10% to 90% of the peak (2.49 K km s^{-1}), with a 10% step. Molecular clouds, LIRS36, LIRS49, SMC–B2, and the star-forming region N27 are labeled. Bottom: HCR LIRS36–east and the two highest contrast HCRs (from 1 to 2 in order of size) overlaid in black contours on the CO(1–0) integrated intensity map.

the highest contrasts are labeled. HCR LIRS36–east, which will be discussed in the next subsection, is also shown in Figure 6.

The most striking feature in Figure 6 is that HCRs are mainly distributed along the edges of CO(1–0) contours. The fact that no HCR is found close to the CO(1–0) peaks is mainly due to our selection effect as CO(1–0) peaks often coincide with H II regions. However, the distribution of HCRs is clearly more extended than the CO(1–0) distribution. The HCR B2–1 is especially interesting. Its morphology follows the CO distribution between molecular clouds SMC–B2 and LIRS49, but along the periphery of the CO peaks. While no obvious decrease in the stellar distribution is seen in the DSS *R*-band image, there is a sharp edge of N27 right where B2–1 starts.

The extended HCR distribution around CO(1–0) peaks is reminiscent of the H$_2$ distribution derived by Leroy et al. (2007). While CO(1–0) and H$_2$ (spatial resolution of 46 pc) were found
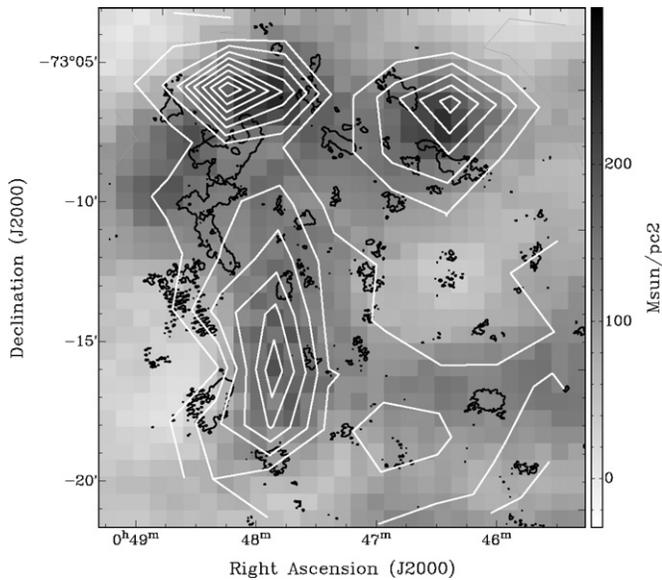
Figure 7. Selected HCRs in the SMC–B2 region overlaid in black contours on the H₂ surface density map of Leroy et al. (2007). CO(1–0) emission from the NANTEN survey (Mizuno et al. 2001) is also overlaid in white contours. The CO contours are from 10% to 90% of the peak (2.49 K km s⁻¹), with 10% step.

to have similar structure in the SW bar region, the H_2 distribution was found to be extended by 30% in the outer parts of SMC molecular clouds. One possible reason for this is the selective photodissociation of CO by the intense radiation field while H_2 survives due to its high self-shielding (e.g., Rubio et al. 1993). We show the selected HCRs overlaid on the H_2 surface density map of Leroy et al. (2007) in Figure 7. The extended HCR distribution is clearly seen in the figure. HCRs avoid the H_2 peaks, which mostly coincide with the CO(1–0) peaks, but are still distributed in regions with $\Sigma_{H_2} = 60$–$180\ M_\odot\ \mathrm{pc}^{-2}$.

Bolatto et al. (2005) analyzed multiple CO line ratios of star-forming regions in the SMC bar and found that high-temperature molecular gas traced by CO(4–3) ($T_{\mathrm{kin}} = 100$–300 K and $n_{H_2} = 10^{2-3}\ \mathrm{cm}^{-3}$) is frequently associated with colder ($T_{\mathrm{kin}} =$

10–60 K) but much denser ($n_{H_2} = 10^{4-5}\ \mathrm{cm}^{-3}$) molecular gas. This suggests that a multi-phase (cold and warm) molecular medium exists in this region. Therefore, the HCR B2–1 may be tracing a moderately dense and warm envelope of the cool SMC–B2 molecular cloud.

The emerging picture from the above two regions is that HCRs most likely trace a moderately dense gas in the outskirts of CO(1–0) clouds, abundant in H_2, but generally weak in CO(1–0) in regions with strong radiation field, and most likely reasonably warm ($T > 10$ K). Since our IR observations have a high-angular resolution of 6″ (or 3 pc), significantly higher than what has been achieved for CO or H_2, HCRs (ranging in size from a few to 50 pc) demonstrate that H_2 gas traced by weak CO emission is clumpy on scales of a few pc in the SMC.

4.3. HCR LIRS36–EAST

This particular HCR is the only one visible by eye as a dark silhouette in the *Spitzer* 24 μm image and has largely motivated our study. The HCR LIRS36–east is located at the east edge of molecular cloud LIRS36 $(\alpha, \delta)_{\mathrm{J2000}} = (00^{\mathrm{h}}:47^{\mathrm{m}}:30^{\mathrm{s}}, -73°:07':30'')$ and near SMC–B2. Figure 8 shows the HCR LIRS36–east seen as a white, finger-like silhouette in the *Spitzer* 24 μm image. White contours are from the NANTEN CO(1–0) Survey (Mizuno et al. 2001).

In Figure 9, we show H_2 (28.2 μm; red), S III (33.5 μm; blue), and 1.2 cm radio continuum (white) emission overlaid on the *Spitzer* 24 μm image. Observations of H_2 and S III were obtained with the Infrared Spectrograph (IRS) on board the *Spitzer* (K. M. Sandstrom et al. 2009, in preparation), while the radio continuum source at 1.2 cm is a detection of SNR J0047.2–7308 from our study (see Section 5.3). SNR J0047.2–7308 is visible in the radio continuum emission, while SNR B0045–7322 (Ye & Turtle 1993) is traced by S III north of HCR LIRS36–east. It is interesting to note the compressed morphology of S III and H_2 contours on both north and south side of HCR LIRS36–east. This morphology is suggestive of the existence of a dense medium associated with HCR LIRS36–east, in agreement with findings for several other HCRs discussed earlier.
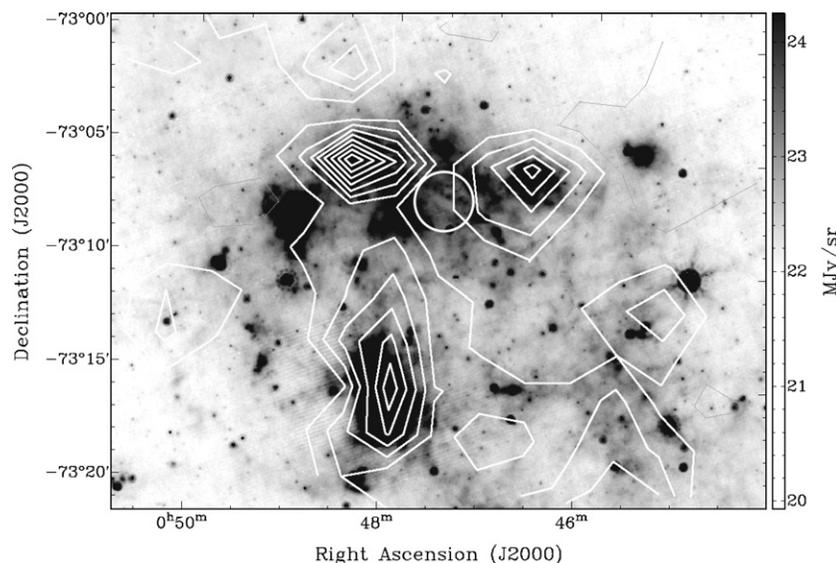
Figure 8. *Spitzer* 24 μm image of the SMC SW bar region. The intensity scale of the image was stretched to emphasize the location of HCR LIRS36–east between molecular clouds LIRS36 and LIRS49. The white contours are from the NANTEN CO(1–0) Survey (Mizuno et al. 2001). The contour levels are from 10% to 90% of the peak (2.49 K km s⁻¹), with 10% step. The primary beam of the ATCA (2′.4 at 23 GHz) is centered on HCR LIRS36–east, $(\alpha, \delta)_{\mathrm{J2000}} = (00^{\mathrm{h}}:47^{\mathrm{m}}:30^{\mathrm{s}}, -73°:07':30'')$, and is shown as a white circle.
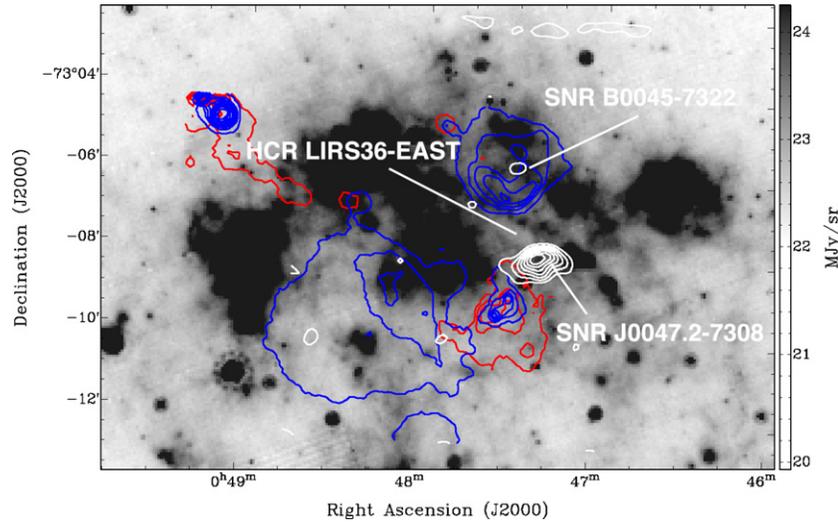
Figure 9. Emission of H_2 at 28.2 μm (red), S III at 33.5 μm (blue), and 1.2 cm radio continuum (white) overlaid on the *Spitzer* 24 μm image of the SMC SW bar region. H_2 and S III data were obtained with the IRS (K. M. Sandstrom et al. 2009, in preparation). The contour levels range from 20% to 90% of the peak (0.16 erg s^{-1} cm^{-2}) for H_2, from 10% to 90% of the peak (2.52 erg s^{-1} cm^{-2}) for S III, and from 30% to 90% of the peak (0.0023 mJy beam^{-1}) for 1.2 cm emission. All contours have a step of 10%.

(A color version of this figure is available in the online journal.)

In addition, Scalise & Braz (1982) detected 6_{16}–45_{23} transition of the water molecule ($\nu = 22.235$ GHz) at a position very close to HCR LIRS36–east $(\alpha, \delta)_{J2000} = (00^h:47^m:31^s, -73°:08':20'')$ with the 14 m Itapetinga Radio Telescope (IRT). While the existence of water molecule in this region will clearly signify dense molecular gas, it is possible that the water maser is associated with one of nearby H II regions since the positional accuracy of the IRT is quite poor (beam size $\sim$3′). In addition, Oliveira et al. (2006) performed 22 GHz observations toward the pointing of Scalise & Braz (1982) with the 64 m Parkes telescope but failed to confirm the water maser detection.

5. SEARCH FOR MOLECULES IN HCR LIRS36–EAST

Based on the estimated properties of HCRs (Section 3), as well as their comparison with observations at other wavelengths, HCRs likely trace reasonably dense molecular gas. To investigate physical properties of this medium, we have undertaken a search for several molecular species in the direction of HCR LIRS36–east. This particular HCR was chosen because of its obvious dark silhouette in the *Spitzer* 24 μm image. In addition, other multi-wavelength data strongly suggest the existence of dense gas in this region. Surprisingly, no spectral lines were detected. In this section, we summarize our observations and estimate upper limits to the column densities of several molecular species. We did detect a radio continuum source at 1.2 cm, corresponding to SNR J0047.2–7308. This finding is discussed in Section 5.3.

5.1. Observations of NH_3 with the ATCA

Observations of (1, 1) and (2, 2) inversion transitions of ammonia (NH_3) were made on 2007 September 26–29 using the Australia Telescope Compact Array (ATCA).[9] Six (effectively five; the sixth antenna is down weighted due to its long baseline) antennas in the H75 configuration were used during the observations. The primary beam of the ATCA in the H75 configuration

at 1.2 cm is 2′.4. The synthesized beam size is 24″.6 × 22″.4. Two intermediate frequencies (IFs) were used to measure both transitions simultaneously. The first IF ($\Delta\nu = 8$ MHz; 102 km s^{-1}) was tuned to the frequency of 23.694 GHz with 512 channels ($\Delta\nu = 16$ kHz; 0.2 km s^{-1}) to sample emission from the (1, 1) transition. The second IF ($\Delta\nu = 16$ MHz; 205 km s^{-1}) was set at the rest frequency of 23.723 GHz with 256 channels ($\Delta\nu = 63$ kHz; 0.8 km s^{-1}) to sample the emission from the (2, 2) transition. As shown in Figure 8, HCR LIRS36–east is well enclosed by the ATCA primary beam and we have used only a single pointing for our observations. The total integration time on the source was 32 hr. PKS 2353–686 was observed every 30 minutes to calibrate the phase and gain. The flux calibration source was PKS 1934–638. Observations of PKS 1921–293 were made to calibrate the bandpass.

The data reduction including flagging, calibration of antenna amplitude and phase was made by using the radio interferometry reduction package, MIRIAD (Sault et al. 1995). We followed the procedure outlined in the MIRIAD manual for 1.2 cm ATCA observations.[10] We achieved a sensitivity of $\sim$1 mJy per synthesized beam per channel for both transitions.

5.1.1. Upper Limits to the Column Density of NH_3

We did not detect emission from the either (1, 1) or (2, 2) transitions. Three-channel Hanning smoothing to reduce the noise per spectral resolution element was also unsuccessful in yielding any detection of emission. Table 1 shows 3σ noise levels in the non-smoothed image.

With 3σ values, we can set upper limits to the optical depths of the (1, 1) and (2, 2) transitions. The upper limits can be determined from the basic radiative transfer equation

$$T_{\mathrm{mb}} = T_{\mathrm{bg}}e^{-\tau} + T_{\mathrm{ex}}(1 - e^{-\tau}), \qquad (2)$$

where T_{mb} is the main beam brightness temperature of each transition, T_{bg} is the background temperature, T_{ex} is the excitation temperature of the observed transition, and τ is its optical

Table 1
Summary of ATCA Observations

Molecule	Transition	Rest Frequency (MHz)	3σ Level[a] (mJy beam^{-1})	NH$_3$ Column Density[b] (cm^{-2})
NH$_3$	(1, 1)	23694.506	3.2	$< 2.7 \times 10^{12}$
NH$_3$	(2, 2)	23722.634	1.7	$< 6.5 \times 10^{11}$

Notes.
[a] Noise levels at central channels for frequency resolutions of 16 kHz and 63 kHz, respectively, for (1, 1) and (2, 2) transitions.
[b] When (A15) of Ungerechts et al. (1986) is used, total ammonia column density, N(NH$_3$) is estimated as 6.2×10^{12} cm^{-2}.

Table 2
Summary of Mopra Observations

Molecule	Transition	Rest Frequency (MHz)	3σ Level[a] (mK)		Column Density (cm^{-2})	
			Pointing 1[b]	Pointing 2[c]	Pointing 1	Pointing 2
N$_2$H$^+$	$J = 1$–0	93173.809	47	42	$< 2.7 \times 10^{12}$	$< 2.4 \times 10^{12}$
HNC	$J = 1$–0	90663.574	35	31	$< 2.9 \times 10^{11}$	$< 2.5 \times 10^{11}$
HCO$^+$	$J = 1$–0	89188.518	48	47	$< 3.5 \times 10^{11}$	$< 3.4 \times 10^{11}$
HCN	$J = 1$–0	88631.847	45	36	$< 1.2 \times 10^{12}$	$< 9.6 \times 10^{11}$

Notes.
[a] Noise levels for an individual channel in the main beam brightness temperature scale.
[b] The position is $(\alpha, \delta)_{J2000} = (00^h{:}47^m{:}24{.}^s6, -73^\circ{:}07'{:}34'')$.
[c] The position is $(\alpha, \delta)_{J2000} = (00^h{:}47^m{:}30{.}^s4, -73^\circ{:}07'{:}28'')$.

depth. Since we have to subtract the continuum emission to be able to detect any line emission over the continuum, an observable quantity T'_{mb} can be defined as $T'_{mb} = T_{mb} - T_c$ where T_c is the brightness temperature of the continuum emission. Furthermore, we assumed that $T_c = T_{cmb} = 2.73$ K. Hence, Equation (2) can be written as

$$T'_{mb} = (T_{ex} - T_{cmb})(1 - e^{-\tau}). \quad (3)$$

To obtain upper limits, we assumed the excitation temperature for the (1, 1) and (2, 2) transitions, $T_{ex} = 20$ K (Frieswijk et al. 2007). The column densities of the (1, 1) and (2, 2) transitions were derived by using the following equations (Mangum et al. 1992):

$$N(1, 1) = 6.60 \times 10^{14} \frac{T_{ex}(2, 2; 1, 1)}{\nu(1, 1)} \tau(1, 1)\Delta v \text{ cm}^{-2},$$

$$N(2, 2) = 3.11 \times 10^{14} \frac{T_{ex}(2, 2; 1, 1)}{\nu(2, 2)} \tau(2, 2)\Delta v \text{ cm}^{-2}, \quad (4)$$

where $\nu(1, 1)$ and $\nu(2, 2)$ are the transition frequencies in GHz, $\tau(1, 1)$ and $\tau(2, 2)$ are the optical depths of the main hyperfine components of the (1, 1) and (2, 2) transitions, and Δv is the velocity width in km s^{-1}. From the recent detection of NH$_3$ in the LMC (Henkel & Ott 2009), we adopted $\Delta v = 5$ km s^{-1}. Table 1 shows the derived upper limits to the column densities of the two transitions.

5.2. Observations of N$_2$H$^+$, HNC, HCO$^+$, and HCN with the Mopra Telescope

Observations of N$_2$H$^+$(1–0), HNC(1–0), HCO$^+$(1–0), and HCN(1–0) lines were made on 2008 May 5–7 using the 22 m Mopra single-dish radio telescope.[11] All four lines are good

tracers of dense and cold gas ($n_{crit} = 10^{5-6}$ cm^{-3}). The zoom mode of the Mopra spectrometer (MOPS) was used for these observations. The bandwidth and resolution of the zoom mode at 90 GHz are 456 km s^{-1} and 0.11 km s^{-1} (137 MHz and 33 kHz), respectively. The beam size of the Mopra telescope at 90 GHz is $\sim 36''$ (Ladd et al. 2005). Observations of two positions with the highest contrasts were performed. The positions of these two pointings are $(\alpha, \delta)_{J2000} = (00^h{:}47^m{:}24{.}^s6, -73^\circ{:}07'{:}34'')$ and $(00^h{:}47^m{:}30.4^s, -73^\circ{:}07'{:}28'')$. The first and second pointings were integrated for 2.6 hr and 2.4 hr, on source, respectively. The system temperature varied from 170 to 260 K during the observations.

The initial data reduction of correcting the spectra for the off-source bandpass, and averaging, was done with the ATNF Spectral line Analysis Package, ASAP.[12] Further data reduction including summing spectra, fitting and subtracting of baseline ripples, and smoothing spectra was done by using generic IDL routines and MPFITFUN (Markwardt 2009). We achieved a sensitivity of ~ 15 mK in the main beam brightness temperature scale per channel for four lines.

5.2.1. Upper Limits to the Column Densities of N$_2$H$^+$, HNC, HCO$^+$, and HCN

We did not detect emission from any of the four lines. Smoothing spectra with 20 channels also failed to yield emission. Table 2 shows 3σ upper limits to the column densities of all transitions. These values were calculated in the Rayleigh–Jeans and optically thin approximation, using the following equation:

$$N = \frac{8\pi W}{\lambda^3 A} \times \frac{g_l}{g_u} \times \frac{1}{J_\nu(T_{ex}) - J_\nu(T_{bg})} \times \frac{1}{1 - \exp(-h\nu/kT_{ex})}$$
$$\times \frac{Q_{rot}}{g_l \exp(-E_l/kT_{ex})}, \quad (5)$$
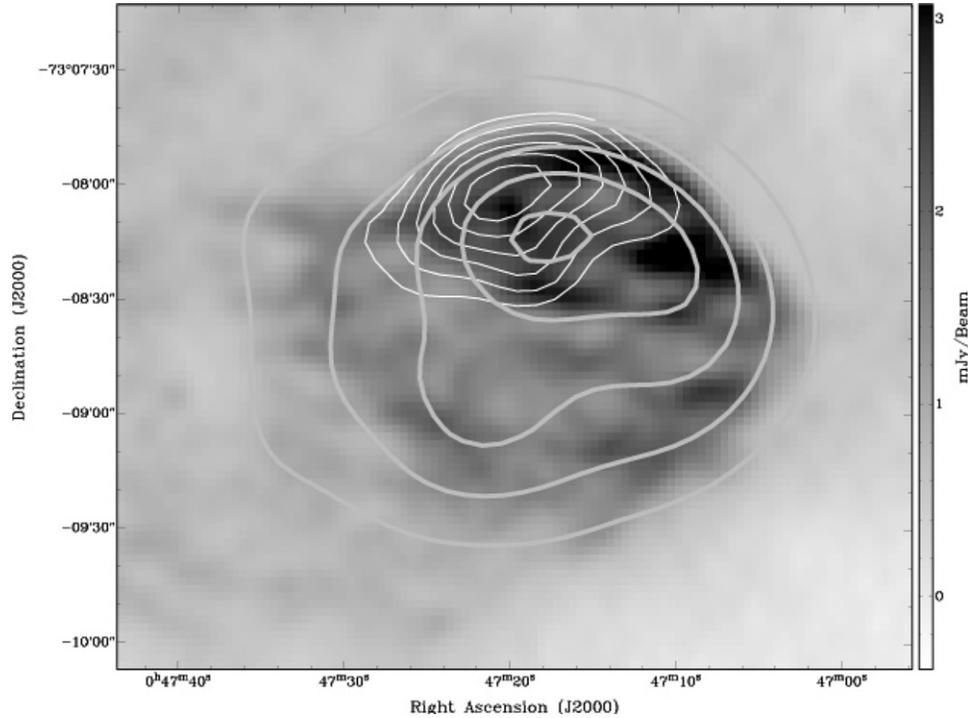
Figure 10. 1.34 GHz image of SNR J0047.2–7308. 4.8 GHz (thick gray), and 1.2 cm (white) emission are overlaid on the image. Images at 1.34 GHz and 4.8 GHz were kindly provided by John Dickel. The contours range from 5% and 90% of the peak (0.2 mJy beam^{-1}) with a step of 2% for the 4.8 GHz emission, and from 40% to 90% of the peak (0.0023 mJy beam^{-1}) with a step of 10% for the 1.2 cm emission. The contours of the 23 GHz (1.2 cm) source follow well the morphology of the SNR at 1.34 GHz and 4.8 GHz, however, its center is offset slightly from the center of the northern rim of the SNR.

where W is the integrated intensity of the line ($W = \pi^{1/2}\Delta v T_{mb}/2\sqrt{ln2}$ for a Gaussian line), λ is the rest wavelength of the transition, A is the Einstein coefficient, g_l and g_u are the statistical weights of the lower and upper levels, $J_\nu(T_{ex})$ and $J_\nu(T_{bg})$ are the equivalent Rayleigh–Jeans excitation and background temperatures, Q_{rot} is the partition function, and E_l is the energy of the lower level from the ground rotational level.

Throughout our calculation, we adopted A and Q_{rot} values from molecular spectroscopy data of the Jet Propulsion Laboratory.[13] $T_{ex} = 20$ K and $T_{bg} = 2.73$ K were assumed for the calculation. $\Delta v = 4$ km s^{-1} was adopted based on observations by Chin et al. (1998) of the nearby molecular cloud LIRS36. Table 2 shows the calculated upper limits to the column densities.

5.3. Detection of Continuum Emission from SNR J0047.2–7308

The only detection in our observations is a radio continuum source at 1.2 cm. The location of the source coincides with the well-known supernova remnant (SNR) in the SMC, SNR J0047.2–7308 (Dickel et al. 2001), centered at $(\alpha, \delta)_{J2000} = (00^h:47^m:17^s, -73°:08':43'')$. While a wealth of data at other wavelengths exists for this SNR, this is the first detection at 1.2 cm. The 1.2 cm continuum image shown in Figure 9 was obtained by summing over all channels in the two ATCA data cubes for the (1, 1) and (2, 2) transitions. The estimated flux density of the SNR at 1.2 cm is 7.4 ± 0.5 mJy.

SNR J0047.2–7308 has been observed at several different radio frequencies (408 MHz: Clarke et al. 1976; 843 MHz: Ye 1988; 1 GHz, 1.34 GHz, and 2.4 GHz: Dickel et al. 2001; 1.42 GHz, 2.37 GHz, 4.8 GHz, and 8.64 GHz: Payne et al. 2004). Figure 10 shows 23 GHz (1.2 cm) and 4.8 GHz radio continuum emission, in white and thick-gray contours, respectively,

overlaid on the 1.34 GHz image. The 1.2 cm continuum source coincides with most of the northern rim of the SNR. On the NE side of the rim, the 1.2 cm contours follow well the morphology of the rim, however, the peak of the 1.2 cm emission is offset slightly ($\sim30''$) from the peak of the northern rim.

Figure 11 shows the radio spectrum of the SNR. Error bars show available flux measurements from the literature at several frequencies. Our flux density measurements at 1.34 GHz, 4.8 GHz, and 23 GHz, obtained only for the area enclosed by the 23 GHz radio emission (which covers most of the northern rim of the SNR), are shown as circles in the same figure. These measurements are very similar to the values from the literature derived for the extent of the whole SNR, suggesting that most of the SNR flux is in its northern rim, as also evident from Figure 10. The solid line in Figure 11 corresponds to the spectral index of -0.6 ± 0.2 and was derived using the measurements from the literature. This spectral index agrees with Payne et al. (2004), and falls within the range expected for SNRs ($-0.8 < \alpha < -0.2$; McGee & Newton 1972).

Curiously, our flux density at 23 GHz is at least a factor of 5 lower than what would be expected for the SNR based on its spectral index. As the largest angular scale we are sensitive to in our observations corresponds to $1'$ and is smaller than the SNR itself (diameter $\sim2'$), it is possible that some flux is missing in our observations, resulting in the underestimated flux density at 23 GHz. In addition, the SNR is located at the south edge of our field of view where we are five times less sensitive than in the image center. We therefore conclude that both missing short spacings and low sensitivity are the most likely reasons for this large departure of the radio spectrum at 23 GHz. An alternative/additional source for this departure could be a spatial variation of the spectral index across the SNR. Dickel et al. (2001) used images at 1.34 and 2.4 GHz to derive the spectral index image of the SNR. Across the SNR, a significant variation can be

[13] http://spec.jpl.nasa.gov/
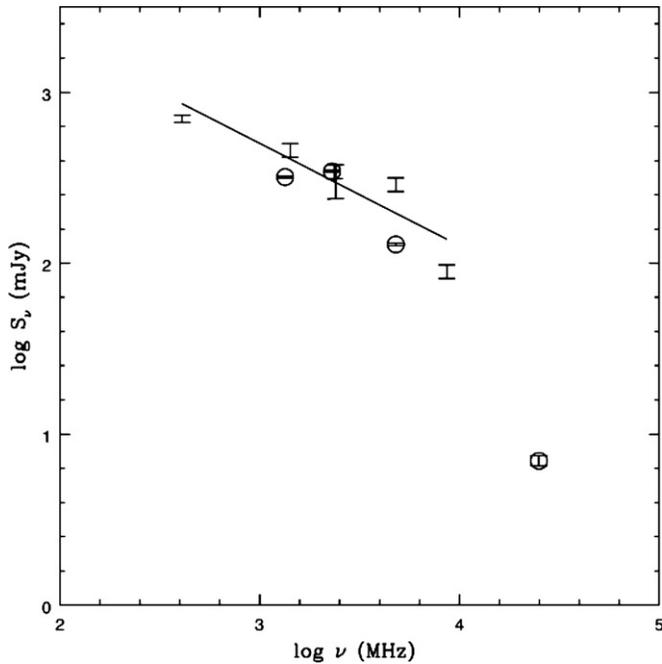
Figure 11. Radio spectrum of SNR J0047.2–7308: S_ν (flux density) in mJy vs. ν (frequency) in MHz. The flux densities at 408 MHz, 1.42 GHz, 2.37 GHz, 2.4 GHz, 4.8 GHz, and 8.64 GHz of the SNR were collected from the literature and are shown with 1σ error bars. Our measurements at 1.34 GHz, 4.8 GHz, and 23 GHz are shown as circles, and encompassed only the portion of the SNR seen at 23 GHz. The spectral index at the lower frequencies (solid line) $\alpha = -0.6 \pm 0.2$ was estimated using the data from literature.

seen in their Figure 4, with the spectral index steepening from $\alpha = -0.4$ close to the center of the SNR, to $\alpha \sim -1$ in several small knots in the northern rim.

6. DISCUSSION

6.1. Comparison with Other Studies of Dark Clouds in the SMC

Dobashi et al. (2009) recently constructed an extinction map of the SMC using the color excess at near-IR wavelengths ($E(J - H)$). They selected ten dark clouds from the $E(J - H)$ map (six in the southern bar, two in the eastern wing, and two in a region just below the northern bar). Similarly to our results, their distribution of dark clouds is similar to that of CO clouds, based on the NANTEN CO(1–0) map. However, their dark clouds, in particular those in the southern bar, frequently coincide with CO peaks, whereas our HCRs are distributed along the peripheries of CO peaks. This difference mainly arises from the fact that our method is blind to high-extinction regions within H II regions, which mostly correspond to strong CO clouds (see Section 2.3). While the two methods are complementary, we emphasize that our spatial resolution is much higher; angular resolution of the $E(J - H)$ map is 2′.6 and thus even the largest HCRs in our study (∼50 pc or ∼2′.9) can hardly be identified.

Dobashi et al. (2009) also provide independent evidence for the nature of the largest HCR found in the N83/N84 region (labeled as 1 in the lower panel of Figure 5; HCR N83/N84–1). This HCR corresponds to their Cloud I. It has $E(J - H) = 0.23 \sim 0.29$ mag or $A_V = 2.51 \sim 3.16$ mag. This is two times higher than our estimate. The most likely cause for this discrepancy is the uncertainty in the position of the HCR/ Cloud I along the line of sight. As we discussed in Section 3, we have assumed that all HCRs are located in the middle of the

SMC, while Dobashi et al. (2009) inferred this quantity from a comparison of the $E(J - H)$ map with a simple model.

6.2. Abundances of Molecular Species

As shown in Table 1, our upper limit to $N(\mathrm{NH_3})$ of HCR LIRS36–east is about 6×10^{12} cm^{-2}. This column density is similar to the only detection of NH$_3$ in the LMC, accomplished very recently with the upgraded ATCA (Henkel & Ott 2009) in the direction of N159–W, one of the most active star-forming regions in the LMC. They found two velocity components in the spectrum and obtained $N(\mathrm{NH_3})$ of $(4.7 \pm 0.5) \times 10^{12}$ cm^{-2} and $(1.1 \pm 0.3) \times 10^{12}$ cm^{-2}, with rotational temperatures of 17 ± 2 K and 15 ± 5 K, respectively. Obviously, our ATCA observations achieved a sensitivity comparable to the NH$_3$ detection in the LMC. However, considering that the SMC has metallicity a few times lower than the LMC, its molecular abundance is expected to be lower in general (e.g., Israel et al. 1993). Future, more sensitive observations are required to probe and constrain the NH$_3$ abundance in the SMC. Up to present, NH$_3$ has not been detected in the SMC.

Our upper limit to $N(\mathrm{NH_3})$ could be significantly underestimated due to the beam dilution if dense molecular clouds are significantly smaller than the ATCA synthesized beam, an effect first pointed out by Osterberg et al. (1997) in their unsuccessful search for NH$_3$ in the Magellanic Clouds. The ATCA beam at 1.2 cm (synthesized beam size $\sim 24''$) corresponds to 7 pc at the distance of the SMC, but dense molecular clumps are likely to be much smaller than the beam. If this is the case, our upper limit to $N(\mathrm{NH_3})$ may be significantly underestimated. If we assume that molecular clumps within our ATCA beam have a size of 1 pc (for example, a dense clump ~ 2 pc in size was observed in the LMC by Wong et al. 2006), then the upper limit to $N(\mathrm{NH_3})$ increases to a few times 10^{14} cm^{-2}.

Our upper limits for other molecular transitions are shown in Table 2. For HCO$^+$, we have achieved an excellent sensitivity. The upper limit to $N(\mathrm{HCO^+})$ is 2–6 times lower than previous measurements obtained in the SMC (Chin et al. 1998; Heikkilä et al. 1999) and at least 10 times lower than any detection of the same molecule in the LMC. Several of earlier SMC and LMC measurements are summarized in Table 3 for a comparison with our results. Similarly to $N(\mathrm{NH_3})$, the upper limit to $N(\mathrm{HCO^+})$ is about 1000 times lower than what is found typically for Galactic IRDCs, but is similar to $N(\mathrm{HCO^+})$ for Galactic diffuse clouds. If we correct for the beam dilution effect (assuming again a cloud size of 1 pc), the upper limit to $N(\mathrm{HCO^+})$ reaches a few times 10^{13} cm^{-2}.

Our upper limits for HCN and HNC are significantly lower than any detections of these molecules in the LMC, but worse (higher) than the two previous detections in the SMC (Chin et al. 1998; Heikkilä et al. 1999). N$_2$H$^+$ was never detected in the SMC and the only detection of this molecule in the LMC has a column density that is three times lower than our upper limit. Our upper limit to $N(\mathrm{HNC})$ is three times higher than the SMC detection in the quiescent molecular cloud LIRS36, but 4–6 times lower than several detections in the LMC. For HCN, the existent SMC detections show large variations in column density, from 1.4×10^{12} cm^{-2} in the star-forming region N27 to 2×10^{10} cm^{-2} in LIRS36. Our upper limit, $< 10^{12}$ cm^{-2}, is significantly lower than any of the LMC detections. Clearly, our upper limits for HNC and HCN are lower than the column densities detected in N27, but higher than detections in LIRS36 and require future, more sensitive observations.

Table 3
N_2H^+, HNC, HCO^+, and HCN Column Densities (Comparison with Other Magellanic Clouds Studies)

Quantities	Our Work	LMC			SMC	
		N159–W[a]	30Dor–10[a]	N113[b]	N27[a]	LIRS36[c]
$N(N_2H^+)$ (cm^{-2})	$< 2 \times 10^{12}$	$\cdots$	$\cdots$	6.3×10^{11}	$\cdots$	$\cdots$
$N(HNC)$ (cm^{-2})	$< 3 \times 10^{11}$	4.7×10^{12}	1.3×10^{12}	2.5×10^{12}	$< 3.7 \times 10^{11}$	9×10^{10}
$N(HCO^+)$ (cm^{-2})	$< 3 \times 10^{11}$	1.4×10^{13}	6.6×10^{12}	4.0×10^{12}	1.9×10^{12}	7×10^{11}
$N(HCN)$ (cm^{-2})	$< 10^{12}$	1.2×10^{13}	4.8×10^{12}	6.3×10^{12}	1.4×10^{12}	2×10^{10}

Notes.
[a] Heikkilä et al. (1999); column densities are obtained from LTE analysis.
[b] Wang et al. (2008).
[c] Chin et al. (1998); column densities are obtained from LTE analysis. $T_{kin} = T_{ex} = 20$ K is assumed.

Our upper limits for HCN, HNC, and HCO^+, which are better than typical LMC detections, confirm that molecular abundances in the SMC are generally lower than in the LMC. In addition, the abundance in both the LMC and SMC can vary spatially by a factor of 10–100. For example, the molecular abundance of the quiescent molecular cloud LIRS36 is significantly lower than the abundance of the star-forming molecular cloud N27. This effect has been reported previously (Heikkilä et al. 1999) and was considered to be due to either metallicity variation and/or ISRF variation. However, it is important to emphasize that molecular multi-line studies of the Magellanic Clouds are still rare and only a handful of measurements exists.

Four molecular species in our study (all except HCO^+) contain nitrogen (N). NH_3 and N_2H^+ were never detected in the SMC, while HCN and HNC were detected only in two molecular clouds. Several authors have noticed a low abundance of N-containing species in the SMC and LMC and have suspected that this is due to a very small nitrogen abundance in these galaxies (e.g., Chin et al. 1998; Wang et al. 2009). It was not clear though whether nitrogen abundance is exceptionally low in the handful of observed molecular clouds, or this is due to chemical processes which operate in all molecular clouds. Future, deeper observations will be required to constrain molecular abundance in HCR LIRS36–east, however, based on our current non-detections its conditions are more similar, or even more extreme, to those of the quiescent molecular cloud LIRS36 than the star-forming cloud N27. The exceptionally low abundance of nitrogen makes the detection of any N-containing molecular species in the SMC extremely hard.

6.3. Constrainst on the Physical Properties of HCRs

What can we learn from our non-detections? Observed molecular species probe gas with a range of physical properties. CO is considered as a good tracer for low-density molecular gas with a molecular hydrogen density $n \sim 10^3$ cm^{-3}, while NH_3 is a good tracer for moderately dense gas with a density of 10^{3-4} cm^{-3}. N_2H^+, HNC, HCO^+, and HCN trace dense and cold gas with $n \sim 10^{5-6}$ cm^{-3}. Our strong upper limit to $N(HCO^+)$, as well as the presence of weak CO(1–0) emission, suggests that the density in HCR LIRS36–east is likely to be $n \sim 10^3$ cm^{-3}. This agrees with the morphological hints in Section 4. Hence, at least one of our HCRs is most likely moderately dense with $n \sim 10^3$ cm^{-3}. This also agrees with the estimated H I + H_2 density of $(0.5–2) \times 10^3$ cm^{-3} based on the H_2 image of Leroy et al. (2007), the H I surface density map of Stanimirović et al. (1999), and assuming a cloud size of $\sim$10 pc.

The hydrogen volume density ($\sim 10^3$ cm^{-3}) of HCRs agrees with the expectation for the cool atomic medium in a low-metallicity environment. For example, Wolfire et al. (1995) es-

timated, based on the heating and cooling equilibrium, that for a dust-to-gas ratio $\sim$30 times lower than in the Galaxy, the cold neutral medium (CNM) and the warm neutral medium (WNM) can co-exist only at a significantly high pressure ($\sim 10^4$ K cm^{-3}). This results in the CNM temperature being as low as 25 K and a volume density being as high as 1.2×10^3 cm^{-3}. Dickey et al. (2000) measured the CNM temperature of 40 K or less in the SMC, in agreement with the Wolfire et al. (1995) prediction. Much of the cold gas in the SMC comes from regions deep inside interstellar clouds, at cold temperatures but high densities, which in the Galaxy would be totally dominated by H_2.

In addition, HCRs appear to have roughly an equal column density of H I and H_2, a few times 10^{21} cm^{-2} (see Section 3). This is consistent with what Dickey et al. (2000) predicted for the transition between H I-dominated and molecule-dominated clouds in the SMC. In the Galaxy, molecular clouds achieve enough self-shielding from the interstellar radiation field at a much lower hydrogen column density, $\sim 4 \times 10^{20}$ cm^{-2} (see Draine & Bertoldi 1996 and references therein). As atomic clouds are converted into molecular clouds, which consequently become fuel for star formation, properties of such transition clouds are important for constraining the process of gas condensation and collapse. We suggest that HCRs are good candidates for future observations with the *Herschel Space Observatory* of species such as neutral carbon (C), which are good tracers of translucent gas.

6.4. Are HCRs Counterparts of Galactic IRDCs?

As pointed out in Section 6.1, our non-detections of various molecular species could be due to significant clumping of molecular gas inside HCRs. In addition, if HCRs are located at the back of the SMC, our extinction values are significantly underestimated. Therefore, we cannot exclude the possibility of HCRs being counterparts of IRDCs found in the Galaxy.

What are the expected molecular abundances for dark clouds in the SMC? The only chemical model that investigated molecular abundances of dark clouds (with $A_V \sim 10$ mag) in the SMC is by Millar & Herbst (1990). This work showed that the abundance of various molecular species does not simply scale with the metal abundance. While the abundance of the N-containing species is often more directly related to the total nitrogen abundance, the abundance of hydrocarbons (like HCO^+) has a more complex dependance on metallicity. In steady state, the abundance of NH_3 is expected to scale roughly with the abundance of nitrogen, while the abundance of HCO^+ is expected to be roughly similar to that in dark clouds in the Galaxy. While the direct model predictions depend heavily on the exact input parameters, we expect that these trends will hold as direct consequences of interstellar chemical reactions. We hence expect the

abundance of NH_3 to be at least 10 times lower in the SMC than in the Galaxy (based on the nitrogen abundance from Millar & Herbst 1990), while the abundance of HCO^+ should be roughly similar in the SMC and the Galaxy.

Galactic IRDCs have $N(NH_3) \sim 10^{15}$ cm^{-2} (Pillai et al. 2006; Frieswijk et al. 2007) and $N(HCO^+) \sim$ a few times 10^{14} cm^{-2} (Purcell et al. 2006). In the case of the SMC, after accounting for the beam dilution effect (due to molecular clumps ~ 1 pc in size), we arrived at the upper limits on $N(NH_3) \sim$ a few times 10^{14} cm^{-2} and $N(HCO^+) \sim$ a few times 10^{13} cm^{-2}. Our upper limit on $N(HCO^+)$ is especially stringent. While our upper limit on the abundance of NH_3 in HCRs is in agreement with what would be expected for IRDCs in the SMC (after accounting for metallicity), the abundance of HCO^+ is at least a factor of 10 lower. We conclude that HCRs are not counterparts of Galactic IRDCs, unless HCO^+ emitting gas contains tiny clumps, ~ 0.5 pc or smaller in size, and/or there are significant spatial variations in metallicity across the SMC. Only future high-resolution observations (e.g., with the Atacama Large Millimeter Array) will be able to investigate this possibility.

6.5. Alternative Explanation for HCRs

An alternative possibility which may be able to explain properties of HCRs involves an anomalous dust abundance yielding an unusually low intensity of 24 μm emission. This would happen if, for example, there are significant spatial variations in the abundance of various dust species. The 24 μm emission in both the SMC and the LMC is dominated by emission from VSGs. In the LMC, the recent *Spitzer* observations have shown regions of 70 μm excess relative to the 24 μm emission (Bernard et al. 2008). The most likely interpretation of this excess is an increased abundance of large VSGs relative to smaller VSGs, which could be caused by erosion of even larger grains by shocks. This illustrates just one of several possible physical processes that could result in an anomalous VSG abundance. Interestingly, the 70 μm excess sources in the LMC do not correlate well with molecular clouds. This is different from HCRs in the SMC where the largest number of objects is found around CO clouds.

To examine the possible anomalous dust abundance in HCRs, we measured flux densities at IR wavelengths provided by the *IRAS* images (Stanimirović et al. 2000) and the *Spitzer* images (Bolatto et al. 2007) for several selected HCRs, including HCR LIRS36–east, HCR B2–1, and HCR N83/N84–1. We examined various flux density ratios; an unusually low value of the 24–160 μm flux density ratio would be an especially good indicator for the deficiency of VSGs relative to the large dust grains. However, we found that the 24–160 μm flux density ratio of several HCRs is similar to the average SMC ratio, suggesting that VSGs are not unusually deficient in HCRs. It is important to emphasize that more detailed measurements of flux ratios are hampered by coarse resolution of IR images at long wavelengths (100 and 160 μm) relative to the 24 μm image. In addition, the proximity of HCRs to bright H II regions makes the background subtraction highly uncertain. Further analysis of the SED of HCRs at long IR wavelengths with higher-angular resolution will be possible with the *Herschel Space Observatory* and would allow us to investigate further this possibility.

7. SUMMARY AND CONCLUSIONS

We have searched for dense ISM in the SMC by applying the unsharp-masking technique to the *Spitzer* 24 μm image. When applied to Galactic IR images, the unsharp-masking technique reveals the highest extinction regions, IRDCs, which are very dense ($n > 10^5$ cm^{-3}) and cold ($T < 25$ K) interstellar clouds. The unsharp-masking technique is limited to regions with diffuse IR background and is blind to dense gas within boundaries of H II regions. As H II regions are often associated with CO peaks, we are not sensitive to molecular gas with substantial CO emission but are mainly tracing a population of interstellar clouds located in the outskirts of CO/H II regions. We call these clouds HCRs and our main results are as follows.

1. We have identified a population of 55 HCRs from the decremental contrast image. HCRs have a highly inhomogeneous spatial distribution, 39 are located in the southern bar, 10 in the northern bar, and 6 in the eastern wing. This distribution is qualitatively similar to the distribution of CO clouds and is suggestive of a possible physical connection between the two populations of clouds. While HCRs with low-contrast values may be spurious detections, this correlation with CO clouds gives us confidence that most HCRs are distinct physical entities.

2. Most identified HCRs have a size of 3–18 pc, which is similar to typical or large Galactic IRDCs. The distribution of peak contrasts (at 24 μm) of HCRs has a peak at 2%–2.5% and this is a factor of 2–3 lower than that of Galactic IRDCs, suggesting only moderately dense environments ($A_V \sim 1$ mag). HCRs in the SMC are less dark than Galactic IRDCs.

3. In the southern bar region, HCRs are mainly distributed in the outskirts of CO clouds and have integrated CO(1–0) intensity of 0.1–0.5 K km s^{-1}. The H_2 surface density map (Leroy et al. 2007), however, suggests they are abundant in H_2 ($\Sigma_{H_2} = 60$–$180\ M_\odot$ pc^{-2}).

4. To constrain the physical properties of HCRs, we have performed NH_3 (with the ATCA), N_2H^+, HNC, HCO^+, and HCN observations (with the Mopra telescope) toward one of HCRs, HCR LIRS36–east. While we did not detect any molecular emission, we achieved excellent sensitivities for NH_3 and HCO^+. Our upper limits to the column density of various molecular species highlight the need for future, more sensitive molecular line observations, especially for N-containing molecules. Our upper limits also place a constraint on the density of HCRs, $n \sim 10^3$ cm^{-3}, suggesting that they are lower density environments than Galactic IRDCs.

5. HCRs appear to trace regions where about half the hydrogen is molecular. Due to the low metal abundance, typical CNM in the SMC (usually traced through 21 cm absorption lines) has temperature similar to what is found for Galactic molecular clouds but much higher density as the multiphase medium can exist only at a higher pressure (Wolfire et al. 1995). The estimated volume density ($\sim 10^3$ cm^{-3}) of HCRs is in agreement with the theoretical expectation for the CNM in an environment with a dust-to-gas ratio about 30 times lower than in the Galaxy. The H I column density, a few times 10^{21} cm^{-2}, suggests that HCRs trace clouds where H_2 is enough shielded against photodissociation. As such clouds are an essential stage for star formation, searching for HCRs in IR images may be a significant way to study early phases of gas condensation in low-metallicity galaxies.

6. Two alternative explanations may account for the observed properties of HCRs. First, HCRs could be counterparts of Galactic IRDCs consisting of very small molecular

clumps (size ~0.5 pc). If only a tiny portion of the cloud surface area produces emission, severe beam dilution may be causing our non-detections of several molecular species. Second, an unusual abundance of dust grains, may result in the absence of emission at 24 μm and appearance of HCRs.

7. We have detected a radio continuum source at 1.2 cm, at a position that corresponds to the northern portion of SNR J0047.2–7308. The measured flux density of the continuum source is 7.4 ± 0.5 mJy. Using the available literature data for frequencies below 10 GHz, we estimated the spectral index of -0.6 ± 0.2. Based on this estimation, the flux density at 23 GHz is at least a factor of 5 lower than what would be expected from an extrapolation of the low-frequency spectral index to 1.2 cm. Some missing short spacings, and poor sensitivity at the position of the SNR, and the possible spatial variation of the spectral index across the SNR can be responsible for the underestimated flux density at 23 GHz.

REFERENCES

Azzopardi, M., Lequeux, J., & Maeder, A. 1988, A&A, 189, 34
Bernard, J.-P., et al. 2008, AJ, 136, 919
Bolatto, A. D., Leroy, A., Israel, F. P., & Jackson, J. M. 2003, ApJ, 595, 167
Bolatto, A. D., Israel, F. P., & Martin, C. L. 2005, ApJ, 633, 210
Bolatto, A. D., et al. 2007, ApJ, 655, 212
Carey, S. J., Clark, F. O., Egan, M. P., Price, S. D., Shipman, R. F., & Kuchar, T. A. 1998, ApJ, 508, 721
Carey, S. J., Feldman, P. A., Redman, R. O., Egan, M. P., MacLeod, J. M., & Price, S. D. 2000, ApJ, 543, L157
Chin, Y. N., Henkel, C., Millar, T. J., Whiteoak, J. B., & Marx-Zimmer, M. 1998, A&A, 330, 901
Clarke, J. N., Little, A. G., & Mills, B. Y. 1976, Austr. J. Phys. Astrophys. Suppl., 40, 1
Dickel, J. R., Williams, R. M., Carter, L. M., Milne, D. K., Petre, R., & Amy, S. W. 2001, AJ, 122, 849
Dickey, J. M., Mebold, U., Stanimirović, S., & Staveley-Smith, L. 2000, ApJ, 536, 756
Dobashi, K., Bernard, J.-P., Kawamura, A., Egusa, F., Hughes, A., Paradis, D., Bot, C., & Reach, W. T. 2009, AJ, 137, 5099
Draine, B. T. 2003, ARA&A, 41, 241
Draine, B. T., & Bertoldi, F. 1996, ApJ, 468, 269
Dufour, R. J. 1975, ApJ, 195, 315
Egan, M. P., Shipman, R. F., Price, S. D., Carey, S. J., Clark, F. O., & Cohen, M. A. 1998, ApJ, 494, L199
Elmegreen, B. G. 1989, ApJ, 338, 178
Frieswijk, W. W. F., Spaans, M., Shipman, R. F., Teyssier, D., & Hily-Blant, P. 2007, A&A, 475, 263
Gordon, K. D., Clayton, G. C., Misselt, K. A., Landolt, A. U., & Wolff, M. J. 2003, ApJ, 594, 279
Groenewegen, M. A. T. 2000, A&A, 363, 901
Heikkilä, A., Johansson, L. E. B., & Olofsson, H. 1999, A&A, 344, 817
Henkel, C., & Ott, J. 2009, in IAU Symp. 256, The Magellanic System: Stars, Gas, and Galaxies, ed. J. Th. van Loon & J. M. Oliveira (Cambridge: Cambridge Univ. Press), 256, PDF–14, http://www.astro.keele.ac.uk/iaus256/proceedings/

Israel, F. P., et al. 1993, A&A, 276, 25
Jackson, J. M., Finn, S. C., Rathborne, J. M., Chambers, E. T., & Simon, R. 2008, ApJ, 680, 349
Kunkel, W. E. 1980, in IAU Symp. 85, Star Clusters, ed. J. E. Hesser (Dordrecht: Reidel), P353
Ladd, N., Purcell, C., Wong, T., & Robertson, S. 2005, PASA, 22, 62
Leroy, A., Bolatto, A., Stanimirović, S., Mizuno, N., Israel, F., & Bot, C. 2007, ApJ, 658, 1027
Leroy, A., et al. 2009, ApJ, 702, 352
Lequeux, J. 1979, A&A, 71, 1
Lequeux, J., Le Bourlot, J., Des Forêts, G. P., Roueff, E., Boulanger, F., & Rubio, M. 1994, A&A, 292, 371
Madden, S. C., Galliano, F., Jones, A. P., & Sauvage, M. 2006, A&A, 446, 877
Mangum, J. G., Wootten, A., & Mundy, L. G. 1992, ApJ, 388, 467
Markwardt, C. B. 2009, arXiv:0902.2850
Mathewson, D. S., Ford, V. L., & Visvanathan, N. 1986, ApJ, 301, 664
Mathis, J. S. 1990, ARA&A, 28, 37
McGee, R. X., & Newton, L. M. 1972, Austr. J. Phys., 25, 619
Millar, T. J., & Herbst, E. 1990, A&A, 231, 466
Mizuno, N., Rubio, M., Mizuno, A., Yamaguchi, R., Onishi, T., & Fukui, Y. 2001, PASJ, 53, L45
Oliveira, J. M. 2009, in IAU Symp. 256, The Magellanic System: Stars, Gas, and Galaxies, ed. J. Th. van Loon & J. M. Oliveria (Cambridge: Cambridge Univ. Press), 191
Oliveira, J. M., van Loon, J. Th., Stanimirović, S., & Zijlstra, A. A. 2006, MNRAS, 372, 1509
Osterberg, J., Staveley-Smith, L., Weisberg, J. M., Dickey, J. M., & Mebold, U. 1997, PASA, 14, 246O
Payne, J. L., Filipović, M. D., Reid, W., Jones, P. A., Staveley-Smith, L., & White, G. L. 2004, MNRAS, 355, 44
Pérault, M., et al. 1996, A&A, 315, L165
Pillai, T., Wyrowski, F., Carey, S. J., & Menten, K. M. 2006, A&A, 450, 569
Purcell, C. R., et al. 2006, MNRAS, 367, 553
Rathborne, J. M., Jackson, J. M., Chambers, E. T., Simon, R., Shipman, R., & Frieswijk, W. 2005, ApJ, 630, L181
Rubio, M., Contursi, A., Lequeux, J., Probst, R., Barbá, R., Boulanger, F., Cesarsky, D., & Maoli, R. 2000, A&A, 359, 1139
Rubio, M., Garay, G., Montani, J., & Thaddeus, P. 1991, ApJ, 368, 173
Rubio, M., Lequeux, J., & Boulanger, F. 1993, A&A, 271, 9
Sault, R. J., Teuben, P. J., & Wright, M. C. H. 1995, in ASP Conf. Ser. 77, Astronomical Data Analysis Software and Systems IV, ed. R. Shaw, H. E. Payne, & J. J. E. Hayes (San Francisco, CA: ASP), 433
Sauvage, M., Vigroux, L., & Thuan, T. X. 1990, A&A, 237, 296
Scalise, E., & Braz, M. A. 1982, AJ, 87, 528
Simon, R., Jackson, J. M., Rathborne, J. M., & Chambers, E. T. 2006a, ApJ, 639, 227
Simon, R., Rathborne, J. M., Shah, R. Y., Jackson, J. M., & Chambers, E. T. 2006b, ApJ, 653, 1325
Stanimirović, S., Staveley-Smith, L., Dickey, J. M., Sault, R. J., & Snowden, S. L. 1999, MNRAS, 302, 417
Stanimirović, S., Staveley-Smith, L., & Jones, P. A. 2004, ApJ, 604, 176
Stanimirović, S., Staveley-Smith, L., van der Hulst, J. M., Bontekoe, T. R., Kester, D. J. M., & Jones, P. A. 2000, MNRAS, 315, 791
Staveley-Smith, L., Kim, S., Putman, M., & Stanimirović, S. 1998, Rev. Mod. Astron., 11, 117
Subramanian, S., & Subramaniam, A. 2009, A&A, 496, 399
Ungerechts, H., Winnewisser, G., & Walmsley, C. M. 1986, A&A, 157, 207
Vangioni-Flam, E., Lequeux, J., Maucherat-Joubert, M., & Rocca-Volmerange, B. 1980, A&A, 90, 73
Wang, M., Chin, Y.-N., Henkel, C., Whiteoak, J. B., & Cunningham, M. 2009, ApJ, 690, 580
Wang, Y., Zhang, Q., Pillai, T., Wyrowski, F., & Wu, Y. 2008, ApJ, 672, L33
Welch, D. L., McLaren, R. A., Madore, B. F., & McAlary, C. W. 1987, ApJ, 321, 162
Werner, M. W., et al. 2004, ApJS, 154, 1
Westerlund, B. E. 1991, in IAU Symp. 148, The Magellanic Clouds, ed. R. Haynes & D. Milne (Dordrecht: Kluwer), 15
Westerlund, B. E., & Glaspey, J. 1971, A&A, 10, 1
Wolfire, M. G., Hollenbach, D., McKee, C. F., Tielens, A. G. G. M., & Bakes, E. L. O. 1995, ApJ, 443, 152
Wong, T., Whiteoak, J. B., Ott, J., Chin, Y.-N., & Cunningham, M. R. 2006, ApJ, 649, 224
Ye, T. 1988, PhD thesis, Sydney Univ.
Ye, T., & Turtle, A. J. 1993, in Lecture Notes in Physics 416: New Aspects of Magellanic Cloud Research, ed. B. Baschek, G. Klare, & J. Lequeux (Berlin: Springer), P167